Advanced Functional Materials

ADVANCED FUNCTIONAL MATERIALS
www.afm-journal.de

RESEARCH ARTICLE OPEN ACCESS

Synergistic Cu-Fe Interactions Enhance Phase Transformation Kinetics Toward High-Performance $CuFeS_2$-Based All-Solid-State Batteries

Changjiang Bai[1] | Katherine A. Mazzio[1,2,3,4] | Florian Ruske[5] | Goutham Srinivas[1] | Tim Bernges[6] | Junwei Meng[7] | Xiangping Min[1] | Yanan Sun[1,2] | Vinita Ahuja[1] | Román Healy Corominas[1] | Volodymyr Baran[8] | Götz Schuck[9] | Michael Haumann[10] | Jürgen Janek[7,11] | Wolfgang G. Zeier[6,12] | Philipp Adelhelm[1,2,13]

[1]Institut für Chemie, Humboldt-Universität zu Berlin, Berlin, Germany | [2]Research Group Operando Battery Analysis (CE-GOBA), Helmholtz-Zentrum Berlin für Materialien und Energie GmbH, Berlin, Germany | [3]Institute of Chemical Technologies and Analytics, TU Wien, Vienna, Austria | [4]X-Ray Center, TU Wien, Vienna, Austria | [5]Solar Energy Division, Helmholtz-Zentrum Berlin für Materialien und Energie GmbH, Berlin, Germany | [6]Institute for Inorganic and Analytical Chemistry, University of Münster, Münster, Germany | [7]Institute for Physical Chemistry & Center for Materials Research, Justus Liebig University, Giessen, Germany | [8]Deutsches Elektronen-Synchrotron DESY, Hamburg, Germany | [9]Department Structure and Dynamics of Energy Materials, Helmholtz-Zentrum Berlin für Materialien Und Energie, Berlin, Germany | [10]Department Atomic-Scale Dynamics in Light-Energy Conversion, XAS@KMC-3 instrument, Helmholtz-Zentrum Berlin für Materialien und Energie GmbH, Berlin, Germany | [11]Center for Materials Research (ZfM), Justus Liebig University Giessen, Giessen, Germany | [12]Institute of Energy Materials and Devices (IMD), IMD-4: Helmholtz-Institut Münster, Forschungszentrum Jülich, Münster, Germany | [13]Center for the Science of Materials Berlin (CSMB), Humboldt-Universität zu Berlin, Berlin, Germany

Correspondence: Katherine A. Mazzio (katherine.mazzio@tuwien.ac.at) | Philipp Adelhelm (philipp.adelhelm@hu-berlin.de)

Received: 7 May 2026 | **Revised:** 7 May 2026 | **Accepted:** 18 May 2026

Keywords: all-solid-state batteries | chalcopyrite | displacement reaction | phase separation | SXRD/XAS/EDX characterization

ABSTRACT

Chalcopyrite ($CuFeS_2$), composed of earth-abundant and environmentally benign elements, was synthesized via solid-state sintering of an equimolar CuS/FeS mixture and evaluated as a cathode material for lithium all-solid-state batteries (ASSBs). $CuFeS_2$ was compared with a mixture of the CuS and FeS parent materials, which are theoretically expected to show similar conversion reaction products during lithiation. Galvanostatic cycling, XRD, XAS, SEM, and EDX analyses revealed that both samples undergo displacement reactions with lithium, leading to phase separation into Cu^0, Fe^0, and Li_2S. However, $CuFeS_2$ exhibits superior reversibility due to the formation of intermediate phases ($LiCuFeS_2$, Li_3CuS_2, Li_2FeS_2), where Cu-related phases may promote uniform Fe reactivation during charging. The synergistic Cu-Fe interactions improve reaction kinetics and reversibility, thereby enhancing overall electrochemical performance. In contrast, the CuS-FeS composite exhibits rapid capacity decay due to independent phase segregation and irreversible Fe^0 passivation. Electrochemically, $CuFeS_2$ delivers 207 mAh g^{-1} with 61% retention after 100 cycles, outperforming CuS-FeS (132 mAh g^{-1}, 40% retention). This work provides the most detailed mechanistic insight to date into the function of $CuFeS_2$ in rechargeable Li cells and shows that controlled intermediate distribution and dynamically evolved conductive networks during phase transformation can improve conversion-type electrodes for ASSBs.

1 | Introduction

All-solid-state batteries (ASSBs) promise higher energy density and improved safety compared to lithium-ion batteries (LIBs) by replacing liquid organic electrolytes with solid electrolytes (SEs) with better mechanical properties and higher Li^+ transference numbers [1]. Numerous cathode active materials (CAMs) have been investigated for LIBs. Among these, layered oxides are widely used due to their favourable electrochemical properties [2, 3]. However, their performance is approaching theoretical limits, and they exhibit drawbacks such as high cost and lattice instability at too high electrode potentials, the latter leading to the release of gaseous O_2 and triggering electrolyte decomposition [4]. These issues are not limited to conventional LIBs, as the decomposition of materials and the degradation of the SE/CAM interfaces are also key challenges in ASSBs [5]. The development of new CAMs that enable stable cycling in ASSBs while using lower cost is therefore of high interest. Transition metal sulfides have attracted increasing attention as alternative CAMs due to their ability to enable reversible "double redox" involving both cations and anions [6]. While the use of sulfides has the drawback of lower redox potentials, these are better aligned with the oxidative stability window of sulfide-based SEs, thereby mitigating severe interfacial degradation [7]. At the same time, they have more favourable mechanical properties than oxides for ASSBs, as they are more deformable and hence the preparation of dense materials with good interface contacts is generally easier [8].

Transition metal sulfides (e.g., CuS [9, 10], FeS [11], TiS_2 [12], FeS_2 [13], etc.) exhibit diverse reaction mechanisms that have been extensively investigated for Li-ion and Na-ion batteries, and are the topic of several recent reviews [14, 15]. These materials demonstrate distinct electrochemical behaviours depending on their composition, structure, and the chosen charge/discharge voltage window, including: intercalation mechanisms (e.g., TiS_2), conversion reactions (e.g., FeS, CuS), and step-wise intercalation/conversion reactions (e.g., FeS_2). While intercalation processes offer high reversibility, they exhibit limited theoretical capacities due to typically low contents of Li^+ intercalation [16]. Conversion reactions, on the other hand, facilitate high capacity by leveraging multi-electron redox of transition metals, but with the drawbacks of severe volume expansion and poor reversibility [17]. Among these systems, Fe-based sulfides are particularly prone to such challenges, often exhibiting pronounced polarization and limited reversibility during cycling [18]. Furthermore, at varying depths of discharge, intercalation and conversion mechanisms can couple to form complex multi-electron transfer pathways. While these stepwise reactions enable high capacity, they also tend to suffer from phase segregation, polarization, and volume instability during cycling [19].

In this work, we address these limitations by introducing Cu into an Fe-based sulfide system, forming $CuFeS_2$ (chalcopyrite) as a model compound to investigate whether cation coupling can modify the reaction pathway and improve electrochemical performance in ASSBs, while also benefiting from the earth-abundance and low cost of Fe [20]. The material was synthesized via solid-state sintering of stoichiometric CuS and FeS precursors. CuS is known to undergo a special type of conversion reaction called a displacement reaction, in which the metallic Cu can migrate over long distances (μm range) during electrochemical cycling, even in ASSBs [21]. While there is surprisingly high reversibility in the Li/CuS system with lower polarization than in other conversion electrodes, there remain kinetic limitations that are at least partially related to the macroscopic displacement of Cu [19]. To this end, Cu is introduced as an electrochemically active component into an Fe-based sulfide system, enabling us to investigate how Cu incorporation influences the reaction environment of Fe and its electrochemical reversibility. Moreover, we find that Cu^+ ions play a crucial role in modulating the electrochemical environment around Fe-phases, thereby improving its activity [22]. After equimolar mixing of CuS and FeS, the ideal lithiation products of $CuFeS_2$ and a mixture of CuS and FeS (herein referred to as CuS-FeS) are identical in the case of full lithiation, as described by Equations (1) and (2).

$$CuFeS_2 + 4Li^+ + 4\,e^- \rightarrow Cu + Fe + 2Li_2S \quad (1)$$

$$CuS + FeS + 4Li^+ + 4e^- \rightarrow Cu + Fe + 2Li_2S \quad (2)$$

However, despite identical overall conversion products, their fundamentally different cation distributions provide a platform to probe how structural integration influences reaction pathways and reversibility. The differential capacity (dQ/dV) analysis reveals fundamentally distinct reaction pathways, with clearly separated voltage plateaus demonstrating independent electrochemical behavior of the CuS and FeS components in the physical mixture. Through comprehensive characterization with XRD, XAS, and SEM-EDX, we were able to identify a critical distinction in the reversibility of their mechanisms. $CuFeS_2$ maintains excellent cycling stability through well-defined intermediate phases ($LiCuFeS_2$, Li_3CuS_2, and Li_2FeS_2). During the initial discharge, Cu and Fe from $LiCuFeS_2$ decomposition remain uniformly distributed. Subsequent discharge leads to confined Cu crystallization within individual particles while maintaining uniform Fe nucleation. The combined electronic and ionic conductivity of Cu and Cu^+ phases facilitates Fe site reactivation during charging, thereby promoting the reversal of the conversion reaction. In contrast, while the CuS-FeS cathode forms some analogous intermediates (Li_3CuS_2 and Li_2FeS_2), severe phase separation between Cu and Fe prevents complete Fe site activation during charging and hence limits cycle life. Our findings demonstrate that precise control of intermediate phase distribution and formation of conductive networks are crucial for optimizing conversion-type electrodes in solid-state batteries.

2 | Results and Discussion

2.1 | Synthesis and Structural Characterization of $CuFeS_2$

Phase-pure $CuFeS_2$ was obtained by the high-temperature solid-state reaction of CuS and FeS precursors. Detailed synthesis procedures are described in the Supporting Information. XRD and Rietveld refinement confirm the phase purity of the synthesized $CuFeS_2$ in an $I\bar{4}2d$ space group (see Figure S1 and Table S1). XPS of $CuFeS_2$ reveals a mixed chemical state comprised of Cu^{2+}/Cu^+, Fe^{3+}/Fe^{2+}, and $S_2^{2-}/2S^{2-}$ (Figure S2). All sieved particles exhibited similar size distributions, as confirmed by both

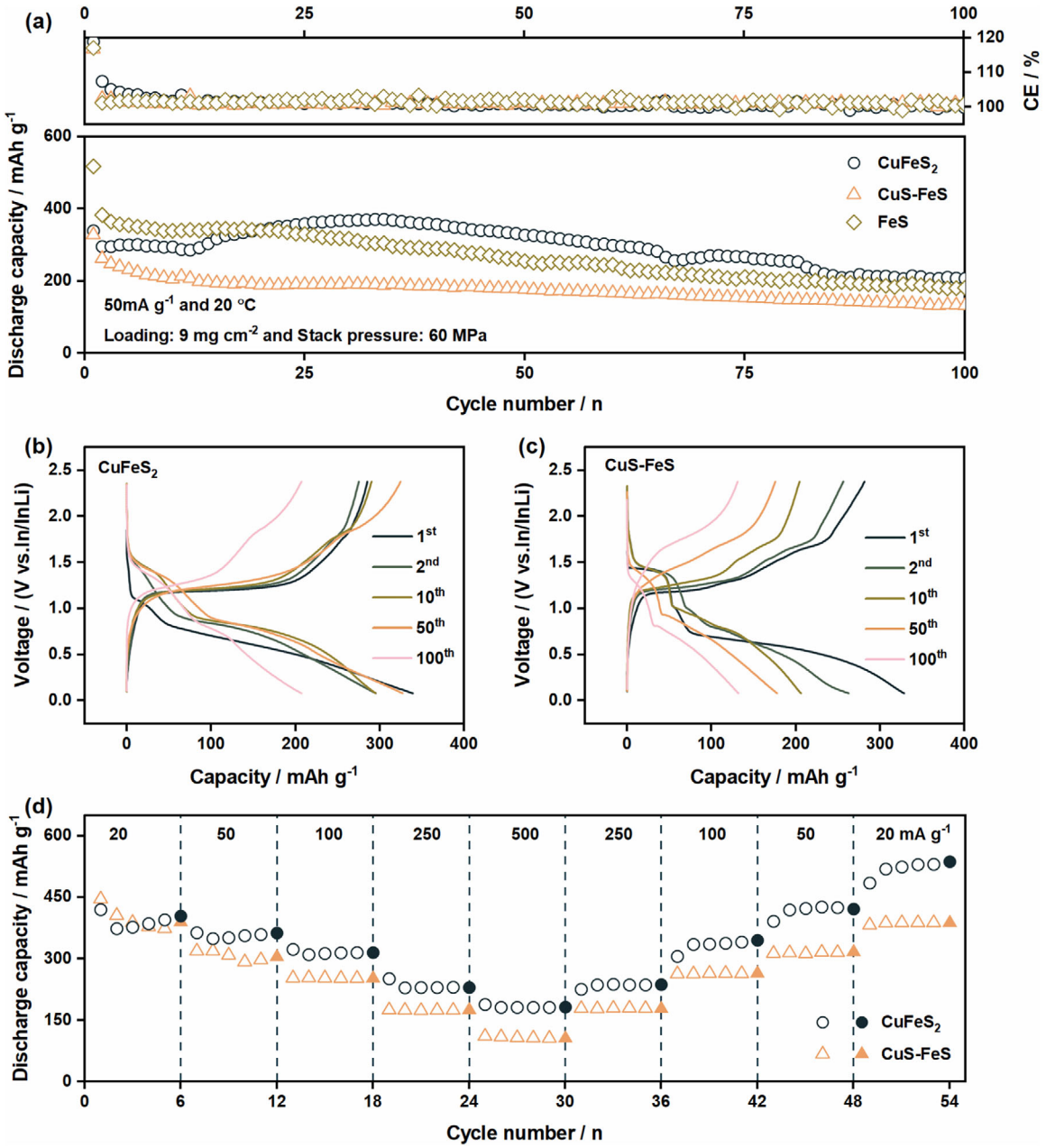

FIGURE 1 | Electrochemical properties of the ASSB [Anode (In/InLi) | $Li_{5.5}PS_{4.5}Cl_{1.5}$ (LPSCl-1.5) | Cathode] with various CAM ($CuFeS_2$, CuS-FeS, or FeS) at 50 mA·g^{-1}, 20°C, and 60 MPa stack pressure. The cathodes contain 55 wt% of CAM, 40 wt% LPSCl-1.5 SEs, and 5 wt% C65 conductive additive. (a) Cycling performance and Coulomb efficiency of $CuFeS_2$, CuS-FeS, and FeS cells. Corresponding voltage profiles for (b) $CuFeS_2$ and (c) CuS-FeS cells showing the first, second, 10th, 50th, and 100th cycles. (d) Rate capability comparison of $CuFeS_2$ vs. CuS-FeS cells at different current densities.

SEM imaging and laser diffraction particle size analysis (15-20 µm range), as shown in Figures S3 and S4. EDX elemental mapping further demonstrated a homogeneous spatial distribution of Cu, Fe, and S throughout the materials, verifying their uniform chemical composition (see Figure S5).

2.2 | Electrochemical Properties of the ASSBs

ASSBs were fabricated with four distinct CAMs: (a) $CuFeS_2$, (b) CuS, (c) FeS, and (d) CuS-FeS composite cathodes with $Li_{5.5}PS_{4.5}Cl_{1.5}$ (LPSCl-1.5) as SE, and all with controlled active material loading of around 9.0 mg cm^{-2}. Assembled cells were cycled between 0.08 and 2.38 V vs. In/InLi at 20°C [23]. Assuming full conversion, the loading corresponds to areal capacity values between 5.0 and 5.5 mAh cm^{-2}, depending on the CAM. All capacity values in this work refer to the total mass of metal sulfide unless otherwise specified. Figure 1a and Figure S7a show data for the Coulomb efficiency (CE), which is here calculated by CE (%) = Q_{dis}/Q_{chg}. Values for the initial Coulomb efficiencies approaching 120% indicate that charging is incomplete. This behavior is typically observed in conversion reactions, particularly for larger particles, and is further enhanced by the solid-state configuration [24]. Stabilization of the Coulomb efficiency at 100%–101% is found in subsequent cycles, reflecting the benefits of an initial discharge activation process. The critical performance metrics

TABLE 1 | Properties of CuS, FeS, and $CuFeS_2$ as CAMs in ASSBs at 25°C.

	CuS	FeS	$CuFeS_2$
$\Delta_r G°$ (kJ mol^{-1})	−378.8	−331.4	−670.1
Number of transferred electrons (n)	2	2	4
Voltage (V vs. Li^+/Li)	1.96	1.72	1.74
Voltage (V vs. In/InLi)	1.34	1.10	1.12
q_{th} by weight (mAh g^{-1})	561	610	587
q_{th} by volume (mAh cm^{-3})	2670	2952	2524
Volume expansion during lithiation (%)	72.3	90.6	62.2
Specific energy density (Wh kg^{-1})	961	906	887
Volumetric energy density (Wh L^{-1})	3037	2663	2708
Conductivity (S cm^{-1})	870 (293K) [9]	50 (333K) [25]	190 (300K) [26]
Mohs hardness	1.8 [21]	4.0 [27]	3.0-4.0 [28]

Note: The thermodynamic data were obtained using the HSC chemistry software database. As these materials do not inherently contain lithium, the theoretical energy density was calculated by considering both the mass and volume of the active material as well as the lithium required to form the fully lithiated products. The calculated volume expansion, specific energy density, and volumetric energy density are summarized in Table S2.

for CuS, FeS, and $CuFeS_2$ as CAMs in ASSBs are summarized in Table 1, including their theoretical capacities, which are comparable across the investigated series. Despite universal capacity fading, all cells demonstrate stable cycling over 100 cycles, with different capacity retentions of CuS (264 mAh g^{-1}, 75% retention) > $CuFeS_2$ (207 mAh g^{-1}, 61%) > CuS-FeS (132 mAh g^{-1}, 40%) > FeS (181 mAh g^{-1}, 35%), directly correlating with their different mechanical stabilities and ionic/electronic conductivities, in both the pristine state and during electrochemical cycling.

Voltage profiles are presented in Figure 1b,c and Figure S7b,c. All materials except FeS exhibited similar initial charge/discharge capacities ($CuFeS_2$: 285/339 mAh g^{-1}; CuS: 320/354 mAh g^{-1}; CuS-FeS: 281/328 mAh g^{-1}), with values ~200 mAh g^{-1} below their theoretical capacities, likely due to their large particle sizes. FeS (442/518 mAh g^{-1}) exhibits a higher initial capacity compared to the other materials, which may be associated with differences in structural evolution during the early cycles. This exposes a greater electrochemically active surface area, particularly in the case of larger particle sizes [29]. Two independently assembled $CuFeS_2$ and CuS-FeS cells were tested for cycling performance (Tables S3 and S4). The voltage profiles of $CuFeS_2$ and CuS-FeS cathodes exhibit distinct first discharge curves that differ markedly from subsequent cycles, which is due to the pristine chemical state of the active materials (e.g., mixed valence in $CuFeS_2$, see XPS of pristine material in Figure S2) that evolves in subsequent cycles. To further elucidate the electrochemical reaction mechanisms, dQ/dV analysis for all four CAMs is shown in Figure S8. $CuFeS_2$ exhibits two broad reduction peaks at 1.1 V and 0.65 V vs. In/InLi, corresponding to its multi-step metal conversion mechanism. However, after the first cycle, these reduction peaks shift to higher potentials and stabilize, suggesting the presence of irreversible reactions during the initial discharge process. During the charging process, two oxidation peaks appear at 1.18 V and 1.78 V vs. In/InLi. The first corresponds to the oxidation of the Cu and Fe metal redox centers, which are expected to overlap, while we attribute the second oxidation process to S redox [30]. CuS exhibits two distinct redox peaks during the initial cycles, corresponding to the sequential redox processes of Cu^{2+}/Cu^+ and Cu^+/Cu^0, although some S redox may also take place [21]. By the 50th and 100th cycles, the oxidation process displays additional peaks. This behavior is attributed to the complexity of the Cu-S phase diagram, which includes multiple binary compounds with varying homogeneity ranges, leading to the formation of diverse intermediate phases during cycling [19, 31]. FeS exhibits a broad single reduction peak during the first cycle, which shifts to a higher potential from the second cycle onward, indicating an irreversible process in the first cycle and/or initial polarization. This type of activation cycle is typical for most conversion electrode materials [15, 32]. During the charging process, a prominent oxidation peak appears at 1.20 V vs. In/InLi, corresponding to the oxidation of Fe^0 [33]. A second, much weaker peak is observed at 1.88 V vs. In/InLi is attributed to a minor transformation of the S chemical state [34]. The mixed CuS-FeS cathode exhibits dQ/dV peaks that simply combine the individual signatures of CuS and FeS, indicating no synergistic electrochemical interactions between the two components. All cathode materials demonstrate measurable electrochemical polarization during cycling.

The rate capabilities of different CAMs were systematically assessed across current densities ranging from 20 to 500 mA g^{-1} (see Figure 1d; Figure S9). At all current rates, $CuFeS_2$ and CuS demonstrated superior cycling stability compared to FeS and CuS-FeS, as evidenced by their higher discharge capacities at each rate. After cycling from 500 to 20 mA g^{-1}, the rate performance followed the same trend and recovered to nearly the original capacity levels. Two independently assembled $CuFeS_2$ and CuS-FeS cells were tested for rate performance (Tables S5 and S6). The rate-dependent behavior primarily reflects differences in conductivity between the CAMs, as evidenced by the increasing polarization in the voltage profiles from 20–500 mA g^{-1} (see Figure S10), which directly correlates with the observed reduction in capacity at higher currents. The comparative electrochemical analysis reveals that while CuS delivers optimal performance due to its superior material properties, with the addition of Fe to form $CuFeS_2$, a high capacity retention is maintained at significantly reduced material costs. Notably, the addition of Cu to

make $CuFeS_2$ enables significantly enhanced capacity retention relative to FeS, highlighting the synergistic advantages of the bimetallic system. $CuFeS_2$ outperforms CuS-FeS composites, demonstrating enhanced cycling stability, despite their similar theoretical conversion reaction products. To further investigate the origin of this improved performance, we examined differences in the reaction mechanisms and morphological changes during electrochemical cycling.

2.3 | Elucidating Reaction Mechanism Differences

2.3.1 | Structural Evolution of $CuFeS_2$ Cathodes by SXRD

Due to distinct electrochemical behavior and capacity differences, ex situ synchrotron XRD (SXRD) was performed to study differences in the reaction mechanisms. Figure 2 shows the SXRD patterns for the $CuFeS_2$ and CuS-FeS cathodes at different charge/discharge states. The SXRD patterns and corresponding voltage profile of the $CuFeS_2$ cathode are shown in Figure 2a, and a representative Le Bail fitting is presented in Figure S11 and Tables S7–S12. At OCV, only $CuFeS_2$ and LPSCl-1.5 are observed, showing the high phase purity of the synthesized $CuFeS_2$ and limited interaction during processing (see Figure S11a and Table S8). The first new crystalline phase appears after the first discharge plateau, where small amounts of $LiCuFeS_2$ are detected alongside predominantly residual $CuFeS_2$ and LPSCl-1.5. In $LiCuFeS_2$, Li occupies the octahedral sites between sulfur layers, and at low lithium concentrations Cu can easily migrate into the tetrahedral sites of this layer as a $Li_{2-x}Cu_xFeS_2$ ($0 \leq x < 1$) solid solution phase [35]. Upon further discharge to 0.9 V, Li_2FeS_2 is found to develop, showing an initial elemental segregation between Cu and Fe species. It should be noted that the Li_2FeS_2 phase is the endpoint of the isostructural $Li_{2-x}Cu_xFeS_2$ phase, and aside from fitting the data, this phase can be visually identified in the diffraction patterns based on the increased intensity at $q = 1.85$ Å^{-1}. Continued discharge to 0.65 V leads to the formation of Li_3CuS_2 and Cu^0 (Figure S11b and Table S9). Assuming only ideal crystalline end-products at this stage leads to an inability to balance the sulfur count strictly with these endmembers. This points toward the presence of an unresolved Fe-containing phase with low sulfur content (e.g., amorphous or nanocrystalline FeS/Fe-rich sulfide domains or heavy antisite disorder), which is further explored by XAS below. At full discharge to 0.08 V, the Cu^0 fraction significantly increases and Li_2S is also found, supporting the overall conversion reaction mechanism. In this case, crystalline Fe^0 is not observed by diffraction, consistent with Fe residing in amorphous/poorly crystalline sulfide domains or as ultrasmall metal clusters below the diffraction detection limit. In the fully discharged state (Figure S11c and Table S10), Le Bail fitting indicates the coexistence of a complex phase mixture of Li_2S, Cu^0, LPSCl-1.5, Li_2FeS_2, Li_3CuS_2, $LiCuFeS_2$, and residual $CuFeS_2$. This phase mixture includes all products associated with the different reaction steps, which is likely attributed to the initially large particle size and significant overpotentials during the electrochemical process. During the charging process, Li_2S is consumed, and the amount of Cu^0 significantly decreases following the first charging plateau at 1.18 V, leaving predominately Li_2FeS_2 and Li_3CuS_2, and some residual Cu^0 crystals. Upon further charging to 1.4 and 2.38 V, the SXRD patterns show the reappearance of $LiCuFeS_2$ and $CuFeS_2$ as the primary phases, coinciding with the complete disappearance of Cu^0 reflections. The presence of mixed phases and low crystallinity in $CuFeS_2$ at full charge (2.38 V) suggests partial irreversibility in the reaction pathway, consistent with the dQ/dV behavior, which shows shifted reduction peaks toward higher potentials after the first discharge process. The second discharge process exhibits voltage plateaus at higher potentials compared to the first cycle. The electrochemical products maintain remarkable consistency with the first discharge process, as evidenced by consistent phase evolution at the different voltage plateaus. Significantly, refinement confirms complete $CuFeS_2$ consumption in subsequent cycles (see Figure S11d and Table S11), demonstrating that initial cycling activates the bulk material over time. After 50 cycles, the cathode is found to undergo a more extensive reaction, with the formation of Li_2S and Cu^0 discharge products, suggesting more sluggish reaction kinetics after long-term cycling (Figure S11e and Table S12).

2.3.2 | Structural Evolution of CuS-FeS Cathodes by SXRD

According to the dQ/dV results, the equimolar CuS-FeS mixture exhibited no synergistic electrochemical behavior between CuS and FeS. The SXRD patterns also reveal the evolution of distinct phases corresponding to CuS and FeS, respectively. The SXRD patterns and corresponding voltage profile of the CuS-FeS cathode are presented in Figure 2b and a representative Le Bail fitting is presented in Figure S12 and Tables S13–S18. Already at OCV there are some unexpected phases when fitting the XRD patterns (see Figure S12a and Table S14). Rather than just containing CuS, FeS, and LPSCl-1.5, there was a small contribution of additional unidentified species. Examining the pristine commercial precursor materials made it clear that these unidentified compounds correspond to additional Fe_xS_y impurities, including FeS_2, and two different phases of Fe_7S_8 (P 31 2 1 and C12/c 1), and these compounds were included in subsequent fittings (see Figure S12b and Table S15). The initial structural changes occur following the first voltage plateau (0.9 V), where CuS converts to α-LiCuS while pristine FeS remains unreacted. Upon further discharge to 0.7 V (second voltage plateau), α-LiCuS undergoes conversion into Cu^0 and Li_3CuS_2, whereas FeS persists in its pristine state. At the first full discharge (0.08 V), a new Li_2S phase emerges (as evidenced by a peak at $q = 1.90$ Å^{-1}), coexisting with Li_3CuS_2 and crystalline Cu^0. Notably, unlike the case of $CuFeS_2$, no Li_2FeS_2 formation is observed in the CuS-FeS cathode during discharge. However, the weakening of FeS reflections suggests its gradual conversion to Fe^0 and Li_2S rather than Li_2FeS_2. Le Bail fitting of the fully discharged state (see Figure S12c and Table S16) confirms a multiphase composition, including Li_2S, Cu^0, LPSCl-1.5, Li_3CuS_2, and residual FeS. While no crystalline Fe was observed after the first discharge, similar to $CuFeS_2$, we can nevertheless anticipate its formation based on the conversion reaction, but this must be confirmed with additional techniques, like XAS as discussed below. The conversion reaction products derived from CuS demonstrate reversibility during the subsequent charging process. Initially, the discharge products (Li_2S and Cu^0) reconvert to Li_3CuS_2 at the first charge voltage plateau (1.2 V). Upon further charging to the second plateau (1.5 V), Li_3CuS_2 transforms into

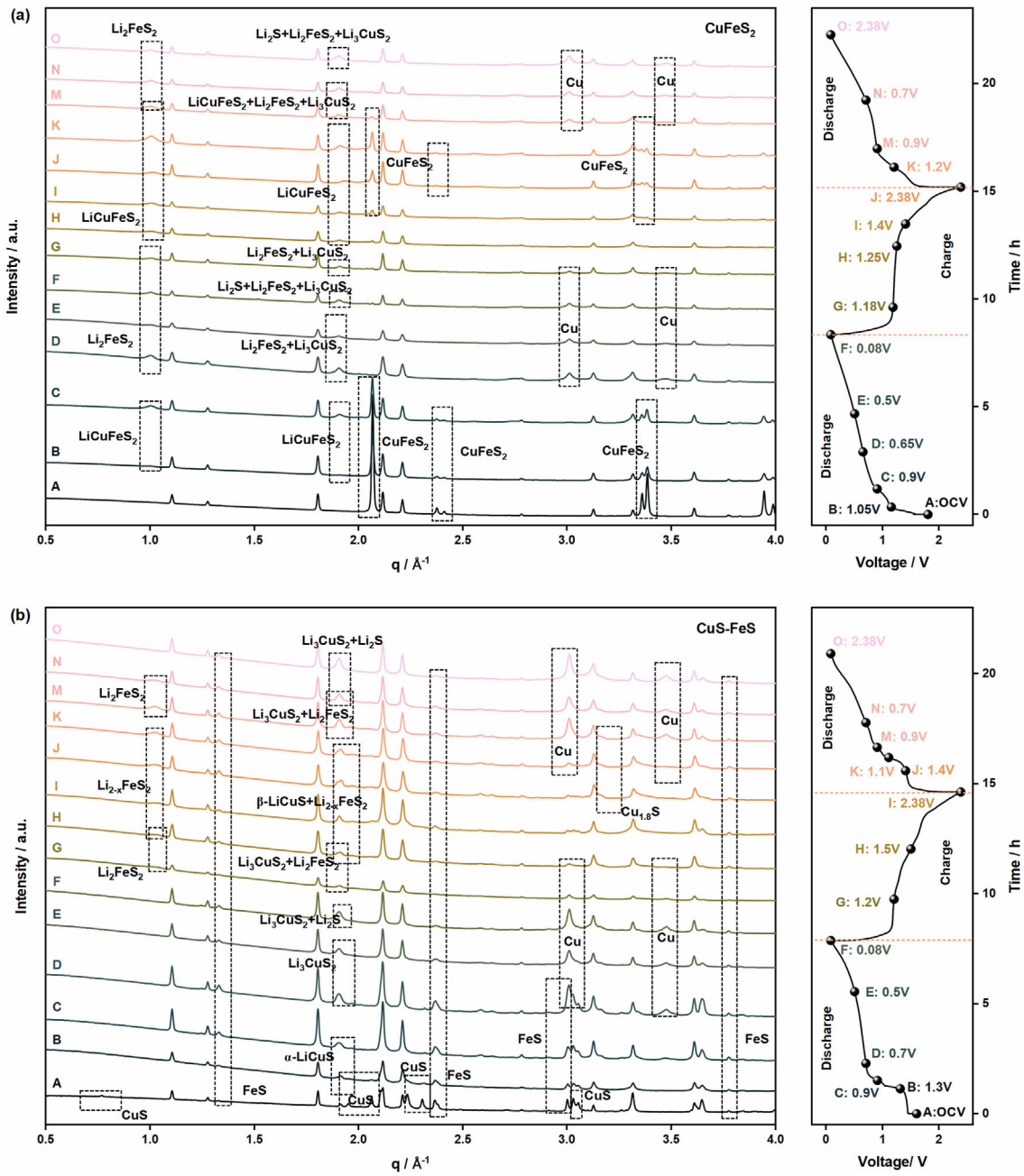

FIGURE 2 | Ex situ synchrotron XRD patterns (SXRD) of (a) $CuFeS_2$ and (b) CuS-FeS cathodes during the first cycle and following second discharge process at different cell voltages when cycled at 50 mA g^{-1}, plotted as a function of scattering vector q ($\lambda = 0.207379$ Å).

β-LiCuS, accompanied by the disappearance of Cu^0. At full charge (2.38 V), partial conversion of β-LiCuS to $Cu_{1.8}S$ is observed, indicating that the original CuS phase is not regained during charging. This is consistent with previous reports [31]. However, the $Li_{2-x}FeS_2$ ($0 < x \leq 1$) phase forms after the first charge plateau and persists throughout the charging process. Even at the fully charged state, the $Li_{2-x}FeS_2$ phase remains detectable, indicating that only a portion of Fe participates in the reaction to form the $Li_{2-x}FeS_2$ layered material, while some Fe loses electrochemical activity. While $Li_{2-x}FeS_2$ demonstrates mixed ionic-electronic conductivity, the progressive electrochemical deactivation of Fe^0 and Li_2S during cycling leads to continuous capacity degradation [36]. This phenomenon directly correlates with the observed cycling instability in FeS-containing cathodes (see Figure 1a; Figure S7). The second discharge process differs fundamentally from the first, as it begins with pre-existing phases (β-LiCuS, $Cu_{1.8}S$, and $Li_{2-x}FeS_2$) rather than pristine CuS and FeS. This compositional difference explains the positive shift in reduction peaks observed in the dQ/dV profiles. While the CuS-derived conversion products show similar behavior between cycles, the $Li_{2-x}FeS_2$ phase undergoes a two-step reaction: first delithiation, followed by conversion to Fe^0 and Li_2S. Interestingly, after the second discharge to 0.08 V, Fe reflections become visible in the SXRD patterns where they were not observed after the first discharge (see Figure S13). Otherwise, the phase composition of the second discharge products matches that of the first discharge, demonstrating consistent electrochemical behavior during subsequent cycles (see Figure S12d and Table S17). After 50 cycles,

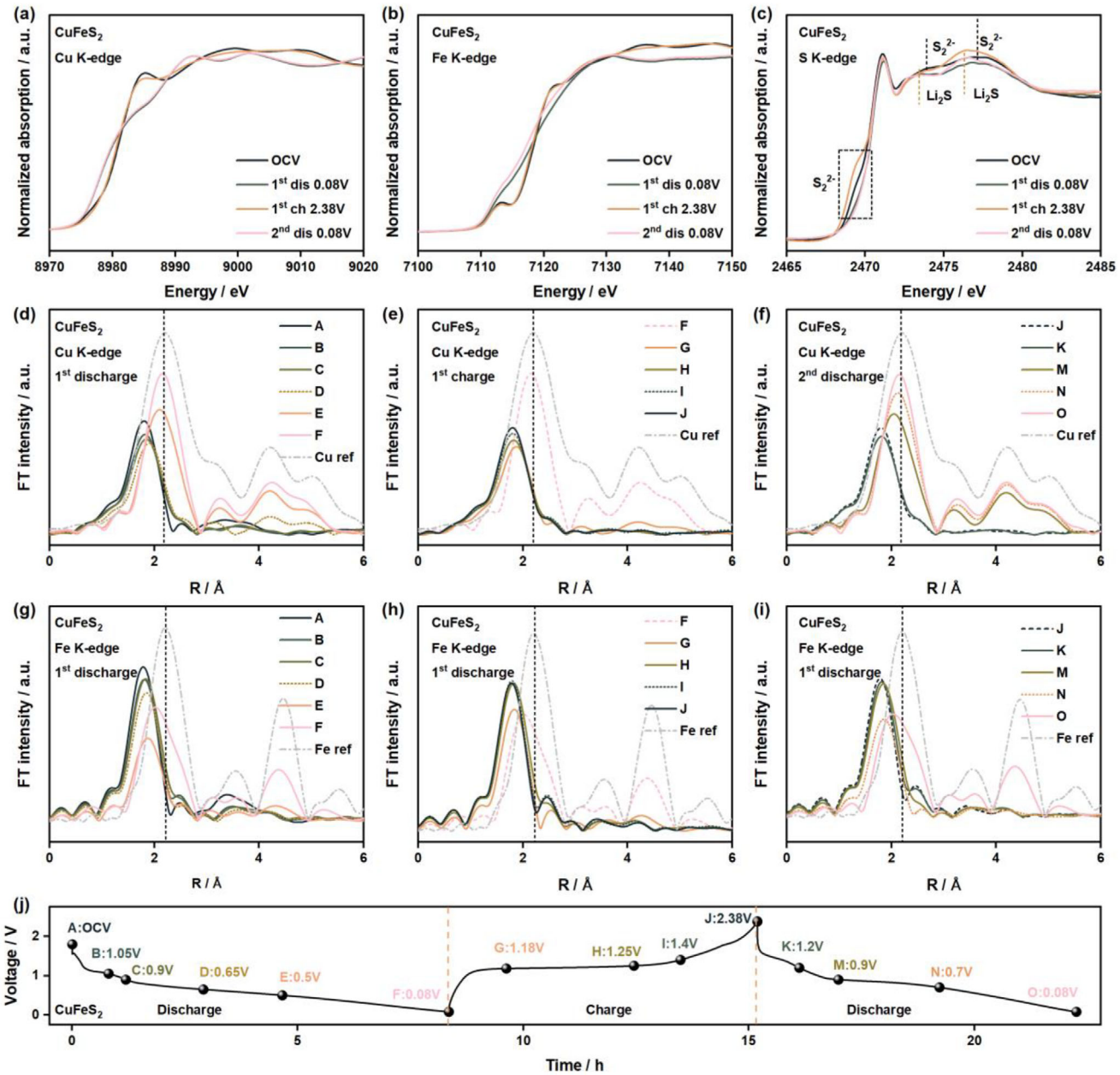

FIGURE 3 | Ex situ XAS spectra of $CuFeS_2$ cathodes. Ex situ XANES spectra for the (a) Cu K-edge, (b) Fe K-edge, and (c) S K-edge for OCV, first discharge to 0.08 V, first charge to 2.38 V, second discharge to 0.08 V. Ex situ Fourier transforms of the EXAFS spectra for the Cu K-edge during the (d) first discharge process, (e) first charge process, and (f) second discharge process. Corresponding Fourier transforms of the EXAFS spectra of the Fe K-edge during the (g) first discharge process, (h) first charge process, and (i) second discharge process. (j) Voltage profile highlighting the different measurement voltages shown in (d-i) for a $CuFeS_2$ cell.

Fe^0 becomes undetectable by SXRD, but FeS remains, suggesting limited reaction kinetics for FeS, possibly due to growth of large and inaccessible domains (see Figure S12e and Table S18).

2.3.3 | Evolution of Oxidation States and Local Structure of $CuFeS_2$ Cathodes by XAS

To further elucidate the reaction mechanism in $CuFeS_2$ and CuS-FeS cathodes, XAS was employed to investigate oxidation state changes and the local structural evolution at the Cu, Fe, and S K-edges. In Figure 3a, the Cu K-edge spectra for $CuFeS_2$ at OCV and the first charge (2.38 V) exhibit slight but measurable changes, suggesting minimal changes in the Cu oxidation state. Meanwhile, the first and second discharge (0.08 V) exhibit strong overlap, indicating a highly reversible electrochemical behavior of the Cu species. In Figure 3b, the same states of charge are shown for the Fe K-edge. At OCV a distinct pre-edge feature at 7113 eV is observed, which is characteristic of tetrahedrally coordinated iron sulfides [37]. This feature reappears after charging to 2.38 V, demonstrating significant structural reversibility. However, the Fe K-edge of the second discharge (0.08 V) shifts to lower energy compared to the first discharge (0.08 V), suggesting sluggish redox kinetics of Fe phases in the initial cycle.

The corresponding EXAFS spectra (Figure 3d–i) reveal that Cu undergoes progressive reduction and Cu—Cu bond formation during discharge, which is fully reversible upon charge. Fe shows the expected solid-solution behavior in $LiCuFeS_2/Li_2FeS_2$ at intermediate potentials and develops reduced Fe domains at deep discharge, consistent with a mixed and highly disordered (amorphous or nanocrystalline) state that remains undetected by SXRD, although contributions from Fe-rich sulfide phases with short-range order cannot be excluded. A comprehensive, voltage-resolved discussion of all Cu, Fe, and S K-edge XANES and EXAFS spectra, including additional intermediate states, is provided in the Supporting Information.

2.3.4 | Evolution of Oxidation States and Local Structure of CuS-FeS Cathodes by XAS

XAS measurements were also performed at the Cu, Fe, and S K-edges for the CuS-FeS cathodes, and the XANES spectra for OCV, first discharge (0.08 V), first charge (2.38 V), and second discharge (0.08 V) are presented in Figure 4a–c. Figure 4a reveals some small but measurable changes in the Cu K-edge spectra between the OCV state and first charge (2.38 V), indicating that while the reaction is largely reversible, there exists a mixture of products during the first cycle. During the first discharge, the Cu K-edge shifts to lower energy, reflecting reduction of Cu species, and a minor offset relative to the second discharge suggests a small degradation of Cu redox activity upon cycling.

In contrast, the Fe K-edge spectra (Figure 4b) show that the distinct pre-edge feature at 7113 eV observed at OCV disappears irreversibly upon charging to 2.38 V, indicating a permanent structural transformation and the formation of new Fe-containing phases. Nevertheless, the first and second discharge spectra overlap strongly, demonstrating reproducible formation of the same Fe-containing discharge products, consistent with the SXRD results. The corresponding Fe K-edge EXAFS evolution reveals minimal Fe participation during the initial conversion of CuS, followed by a sharp decrease in the amplitude of the EXAFS spectra at 0.7 V as Fe—S bonds break and FeS begins to be amorphized. At deeper discharge, the EXAFS spectra show increased Fe-S distances and the appearance of higher-R features, suggesting the formation of partially lithiated FeS_x intermediates and, ultimately, reduced Fe-containing domains within a mixed and structurally disordered state. The low amplitude of the longer-distance EXAFS features indicates limited structural order (amorphous or nanocrystalline character), in agreement with the absence of corresponding reflections in SXRD. During charging, contraction of the Fe-S coordination at the first voltage plateau marks substantial structural reconstruction toward $Li_{2-x}FeS_2$, although further charging leads to only partial reformation of FeS. The second discharge proceeds with more gradual changes in Fe-S coordination and higher overall EXAFS intensities, demonstrating improved reversibility and increased Fe^0 crystallinity at full discharge, again consistent with SXRD. The S K-edge XANES (Figure 4c) further confirm these redox processes. The discharged state (0.08 V) exhibits two broad peaks characteristic of Li_2S formation. In the second discharge, these features shift slightly to higher energy, suggesting a more complete conversion, possibly facilitated by improved electronic conductivity in $Li_{2-x}FeS_2$ [38]. In contrast, the spectra at OCV and after the first charge (2.38 V) exhibit broad peaks near 2473.6 and 2477.0 eV, showing features corresponding to S_2^{2-} and S^0 species at systematically lower energies than those in $CuFeS_2$, consistent with the oxidation of sulfur to higher valence states ($S_2^{2-} \rightarrow S^0$) during charge and confirming the electrochemical generation of defective $Cu_{1.8}S$ and elemental sulfur.

Taken together, these XAS results confirm that Fe in the CuS-FeS composite undergoes a two-step electrochemical process: (i) an initial conversion from FeS to Fe^0 and Li_2S during the first discharge, followed by (ii) partial reversibility through formation of $Li_{2-x}FeS_2$ during charge. However, unlike in $CuFeS_2$, the Fe redox process in CuS-FeS remains largely decoupled from that of Cu, and no synchronous phase transformation is observed. The formation and stabilization of $Li_{2-x}FeS_2$ during cycling leads to partial Fe electrochemical activity loss and structural hysteresis, consistent with the progressive capacity fade observed electrochemically. The stronger Fe^0 features and enhanced reversibility during the second discharge indicate that prior structural reorganization facilitates more complete conversion, but at the expense of increasing heterogeneity and phase segregation during cycling. These results indicate that the distinct intermediate phase evolution between $CuFeS_2$ and CuS-FeS is fundamentally governed by their intrinsic structural characteristics. Specifically, the single-phase $CuFeS_2$, with homogeneous cation distribution, enables continuous formation of intermediate phases throughout the matrix, whereas the phase-separated CuS-FeS mixture leads to spatially confined reactions within individual particles.

2.3.5 | Morphological and Elemental Evolution of $CuFeS_2$ and CuS-FeS Cathodes by SEM/EDX

The XAS results clearly demonstrate the oxidation state changes and local structural evolution during electrochemical cycling. The $CuFeS_2$ cathode maintains superior structural stability and reversibility, as evidenced by the highly reversible changes in both XANES and EXAFS spectra. Moreover, Cu and Fe species in $CuFeS_2$ undergo phase conversion simultaneously at similar potentials. In contrast to the synchronous redox behavior in $CuFeS_2$, the CuS-FeS system demonstrates decoupled phase evolution for Cu and Fe species. This distinct behavior is directly reflected in the markedly different evolution of the Fe-EXAFS spectra in CuS-FeS compared to $CuFeS_2$ during cycling, which reflects their phase-separated electrochemical responses. It is noteworthy that despite these differences in reaction pathways, the phenomenological analysis of the EXAFS spectra indicates the formation of Fe^0 at low discharge (0.08 V) in both cathode systems. Although the reaction pathways have been clearly elucidated, the underlying mechanisms governing the mechanical evolution during the conversion reaction are still not fully understood. To further elucidate the origin of these distinct electrochemical and structural behaviors, the morphological and elemental evolution of the cathodes was examined by SEM and EDX mapping. These analyses provide insight into particle-level changes, element redistribution, and phase separation phenomena accompanying the conversion reactions.

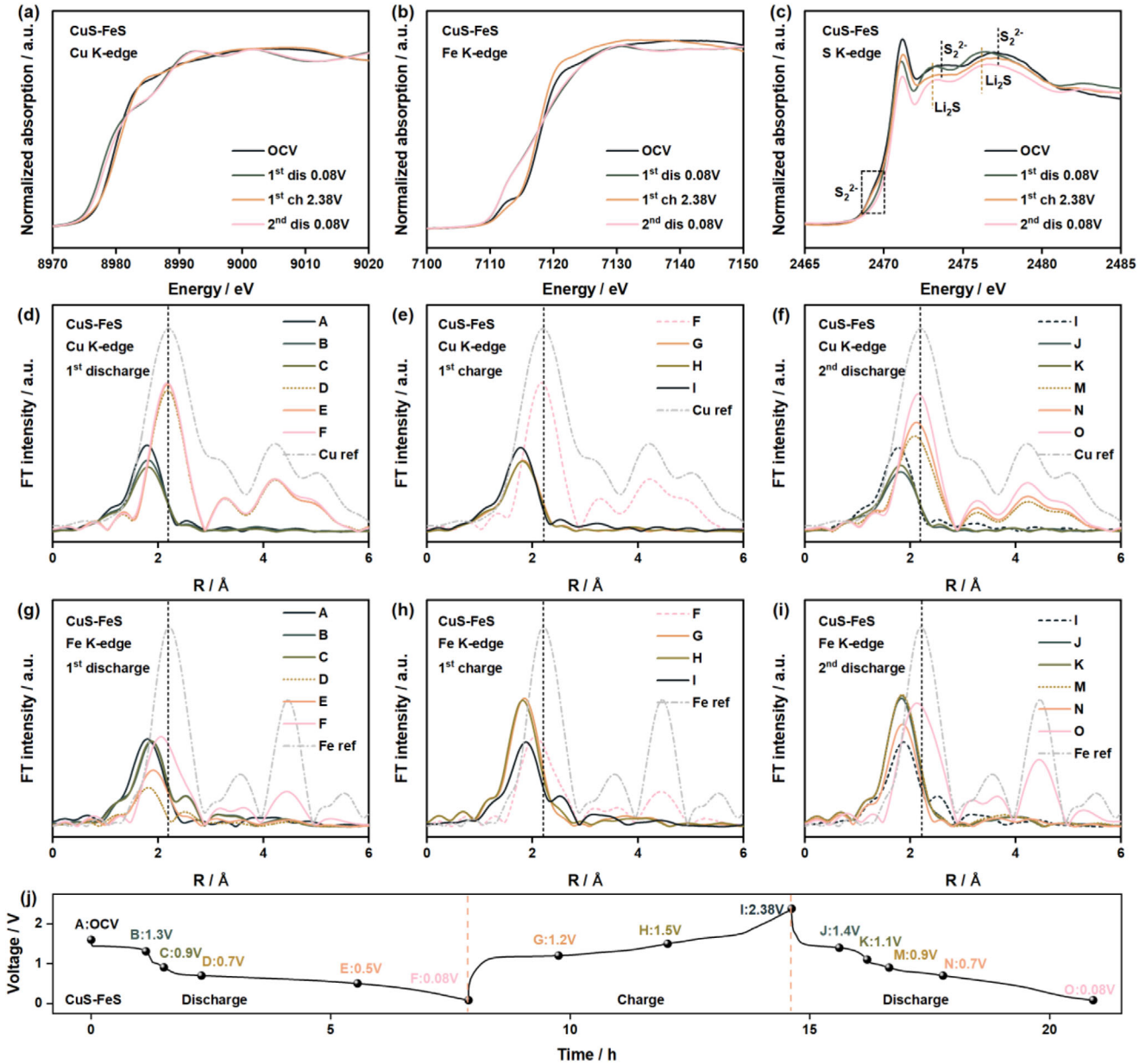

FIGURE 4 | Ex situ XAS spectra of CuS-FeS cathodes. Ex situ XANES spectra for the (a) Cu K-edge, (b) Fe K-edge, and (c) S K-edge for OCV, first discharge to 0.08 V, first charge to 2.38 V, second discharge to 0.08 V. Ex situ Fourier transforms of the EXAFS spectra of Cu K-edge: (d) first discharge process, (e) first charge process, and (f) second discharge process. Ex situ Fourier transforms of the EXAFS spectra of Fe K-edge: (g) first discharge process, (h) first charge process, and (i) second discharge process. (j) Voltage profile highlighting the different measurement voltages shown in (d-i) for a CuS-FeS cell.

SEM imaging and EDX mapping (Figure 5) reveal distinct morphological and elemental evolution in the two cathode systems. In $CuFeS_2$, Cu and Fe are initially co-localized within the same particle domains at OCV. During the first discharge, some Cu is observed to remain with Fe distributed within the CAM particle matrix, while bright Cu spots are found to segregate into discrete metallic domains, demonstrating reversible phase separation. Upon charging, Cu redistributes, restoring a uniform Cu-Fe distribution, and the second discharge reproduces this reversible behavior. After extended cycling (50 cycles), Cu exhibits broader migration beyond the initial particle boundaries and into adjacent regions of the solid electrolyte, while Fe remains localized, indicating strong synergistic coupling that stabilizes the composite structure. In contrast, the CuS-FeS composite displays persistent phase separation where Cu undergoes pronounced aggregation into metallic domains during discharge, whereas Fe retains a homogeneous distribution within individual particles throughout cycling. Long-term cycling shows continued Cu migration, but Fe remains largely segregated. These observations corroborate the decoupled redox behavior revealed by XAS and SXRD and highlight how particle-scale phase segregation and elemental migration govern the differing electrochemical performance and cycling stability of the two systems. Further discussion including representative EDX spectra,

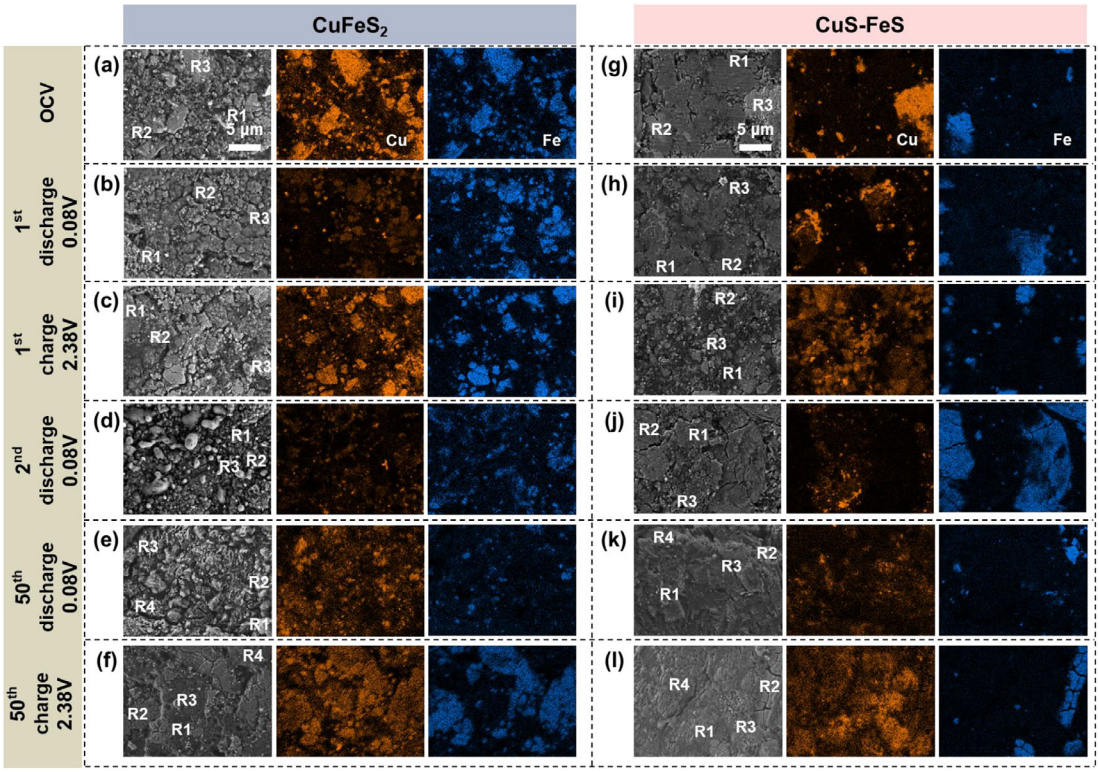

FIGURE 5 | Top-view SEM images and corresponding EDS elemental mapping of Cu and Fe in $CuFeS_2$ and CuS-FeS electrodes at various electrochemical states. For $CuFeS_2$: (a) OCV, (b) first discharge (0.08 V), (c) first charge (2.38 V), (d) second discharge (0.08 V), (e) 50^{th} discharge (0.08 V), and (f) 50^{th} charge (2.38 V). For CuS-FeS: (g) OCV, (h) first discharge (0.08 V), (i) first charge (2.38 V), (j) second discharge (0.08 V), (k) 50^{th} discharge (0.08 V), and (l) 50^{th} charge (2.38 V).

region-of-interest (ROI) analyses, and detailed mapping of minor elements (P, Cl, S) are provided in Supporting Information and Figures S19–S25.

2.4 | Reaction Pathways of $CuFeS_2$ and CuS-FeS Cathodes

The electrochemical reactions in ASSBs are frequently hampered by polarization and inadequate interfacial contact, leading to incomplete conversion and a mixture of residual and intermediate products. Our analysis delineates the actual reaction pathways for $CuFeS_2$ and CuS-FeS cathodes (Figure 6a,b). Furthermore, a key finding is that the CuS-FeS cathode follows a different mechanism in the first discharge process than in the following cycles. These results clearly reveal that Cu and Fe species undergo progressive phase separation into increasingly larger domains during cycling. However, $CuFeS_2$ maintains superior structural stability, with Cu and Fe remaining homogeneously distributed within the entire particle domain. This bulk-scale atomic integration enables synergistic effects, where the combined electronic and ionic conductivity of Cu and Cu^+ phases help to maintain the Fe redox activity during cycling. In contrast, the CuS-FeS system exhibits complete phase segregation between Cu and Fe species, leading to electrochemically isolated Fe domains that readily lose their redox activity. This structural separation, coupled with the formation of defective $Cu_{1.8}S$ and the irreversible passivation of Fe active sites, results in severe and rapid capacity degradation during cycling.

3 | Conclusion

$CuFeS_2$ was synthesized via solid-state sintering of an equimolar CuS-FeS mixture. Both $CuFeS_2$ and the equimolar CuS-FeS composite were used as active materials to assemble ASSBs. By combining galvanostatic cycling, XRD, XAS, SEM, and EDX analyses, we found that both materials undergo a displacement reaction with lithium, resulting in the macroscopic phase separation of Cu^0, Fe^0, and Li_2S. However, a key difference lies in their reversibility: $CuFeS_2$ achieves a much more reversible cycling through intermediate products such as $LiCuFeS_2$, Li_3CuS_2, and Li_2FeS_2. During the initial discharge, Cu and Fe species from $LiCuFeS_2$ decomposition remain uniformly distributed within the particle domain. Upon further discharge, Cu aggregates into crystalline domains confined to individual particles, while Fe nucleates uniformly within a single particle. During charging, the combined electronic and ionic conductivity of Cu-related phases activate Fe reaction sites, enabling highly reversible conversion. In contrast, although the CuS-FeS cathode forms similar intermediates (Li_3CuS_2 and Li_2FeS_2), pronounced phase separation between Cu and Fe species inhibits the activation of some Fe sites. This structural segregation, combined with the formation of defective $Cu_{1.8}S$ and irreversible passivation of Fe active sites, leads to rapid capacity degradation compared to $CuFeS_2$. The electrochemical performance further underscores the superiority of $CuFeS_2$, which delivers a capacity of 207 mAh g^{-1} with a retention of 61.0% after 100 cycles, significantly outperforming the CuS-FeS phase mixture (132 mAh g^{-1} and 40.2% over the same period). At the same time, $CuFeS_2$ shows

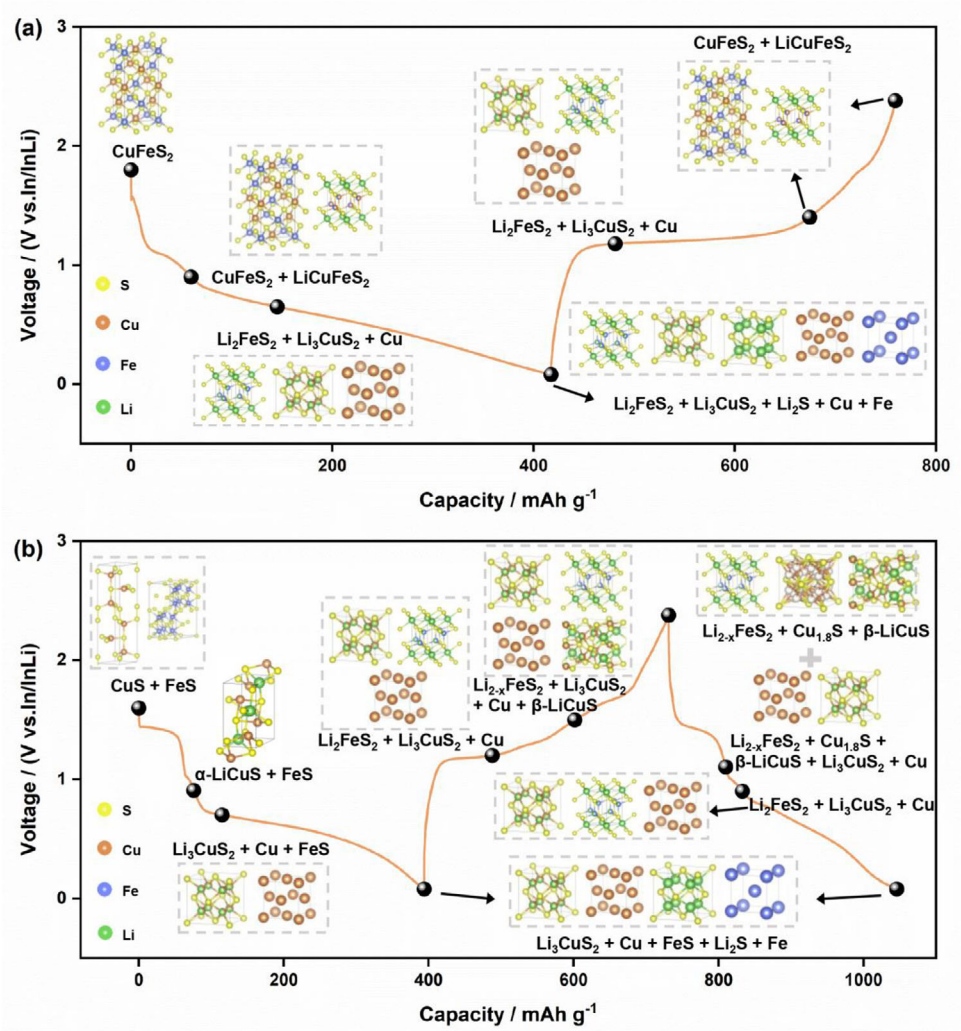

FIGURE 6 | Reaction pathways of $CuFeS_2$ and CuS-FeS cathodes for the initial cycles. The actual phase evolution of (a) $CuFeS_2$ and (b) CuS-FeS cathodes during the discharge/charge process. Residual FeS always exists in the CuS-FeS cell. Therefore, the FeS crystal structure is not shown for other electrochemical states in the figure. The figure was drawn with reference to the illustration reported by Zou et al. [31].

enhanced rate performance, which can be attributed to the synergistic interaction between Cu and Fe compounds.

This study demonstrates that displacement reactions in the solid state can be fairly stable in solid-state cells despite showing large volume changes. The $CuFeS_2$ cathode avoids complete phase separation in the mixed state, while the combination of Cu and Fe has the added benefits of cost reduction and enhanced Fe activity. These findings provide the most detailed understanding to date of the reaction mechanism of $CuFeS_2$ in rechargeable Li cells and propose an effective strategy for regulating intermediate-product distribution and introducing highly conductive active components toward high-performance ASSBs.

Author Contributions

C.J.B., K.A.M., and P.A. conceived the idea, C.J.B. synthesized and characterized the materials, and performed all electrochemical measurements. Ex situ SXRD measurements were done by C.J.B., G.S., and K.A.M. with the help of V.B. Cu and Fe XAS experiments were performed by C.J.B., K.A.M., and X.P.M. with the help of G.S. S K-edge XAS was measured by C.J.B., K.A.M., Y.N.S., V.A., R.H.C., and X.P.M. with the help of M.H. and G.S. SEM/EDX measurements were done by C.J.B. and F.R. XPS measurements were done by J.W.M. and J.J. The SE was synthesized and provided by the T.B. and W.G.Z. The data and manuscript were organized by C.J.B. and K.A.M. The manuscript was written by C.J.B., K.A.M., and P.A. with contributions from all authors.

Acknowledgements

P.A., K.A.M., J. M., J. J., T. B., and W. G. Z. acknowledge support from the project KAROFEST (No. 03XP0498) funded by the Bundesministerium für Forschung, Technologie und Raumfahrt (BMFTR). C.J.B. thanks the China Scholarship Council (CSC) for funding. The authors acknowledge DESY for the beamtime allocation at the P02.1 end-station. Beamtime was allocated for proposals I-20230465. C.J.B. and K.A.M. acknowledge DESY (Hamburg, Germany), a member of the Helmholtz Association HGF, for the support with travel costs. XAS was carried out at the KMC-2 and KMC-3 beamlines at the BESSY II electron storage ring operated by the Helmholtz-Zentrum Berlin für Materialien und Energie GmbH. The authors thank the Helmholtz-Zentrum Berlin für Materialien und Energie GmbH for the allocation of synchrotron radiation beamtime. Beamtime was allocated for proposals 232-12412-ST and 242-12901-ST.

The electron microscopy CoreLab (CCMS) at HZB is acknowledged for providing access to instrumentation. The authors acknowledge the TU Wien Bibliothek for financial support through its Open Access Funding Programme.

Open Access funding provided by Technische Universitat Wien.

Conflicts of Interest

The authors declare no conflicts of interest.

Data Availability Statement

The data that support the findings of this study are available from the corresponding author upon reasonable request.

References

1. A. Banerjee, X. Wang, C. Fang, E. A. Wu, and Y. S. Meng, "Interfaces and Interphases in all-Solid-State Batteries with Inorganic Solid Electrolytes," *Chemical Reviews* 120 (2020): 6878–6933, https://doi.org/10.1021/acs.chemrev.0c00101.

2. S. Puls, E. Nazmutdinova, F. Kalyk, et al., "Benchmarking the Reproducibility of all-solid-state Battery Cell Performance," *Nature Energy* 9 (2024): 1310–1320, https://doi.org/10.1038/s41560-024-01634-3.

3. H. Liu, Y. Ji, Y. Li, et al., "Regulating Lithium Affinity of Hosts for Reversible Lithium Metal Batteries," *Interdisciplinary Materials* 3 (2024): 297–305, https://doi.org/10.1002/idm2.12153.

4. P. K. Nayak, L. Yang, W. Brehm, and P. Adelhelm, "From Lithium-Ion to Sodium-Ion Batteries: Advantages, Challenges, and Surprises," *Angewandte Chemie International Edition* 57 (2018): 102–120, https://doi.org/10.1002/anie.201703772.

5. P. Minnmann, F. Strauss, A. Bielefeld, et al., "Designing Cathodes and Cathode Active Materials for Solid-State Batteries," *Advanced Energy Materials* 12 (2022): 2201425.

6. Z. Zhang, R. Wang, K. A. Mazzio, N. Koch, and P. Adelhelm, "Silver Thiophosphate (Ag_3 PS_4) as a Multielectron Reaction Active Material for Lithium Solid-State Batteries," *Energy Technology* 12 (2024): 2401040.

7. H. Yang, L. Weckelmann, B. Wu, et al., "Sulfide-Based Electrolytes for all-Solid-State Sodium Batteries," *Advanced Energy Materials* (2026): 05208, https://doi.org/10.1002/aenm.202505208.

8. B. Fan, W. Chen, K. Li, et al., "Synergistic Adsorption and Catalytic Effects of Ti_3 C_2 T_X /CoO/MoO_3 Composite on Lithium Polysulfides for High-Performance Lithium–Sulfur Batteries," *Interdisciplinary Materials* 3 (2024): 726–737, https://doi.org/10.1002/idm2.12178.

9. B. Jache, B. Mogwitz, F. Klein, and P. Adelhelm, "Copper Sulfides for Rechargeable Lithium Batteries: Linking Cycling Stability to Electrolyte Composition," *Journal of Power Sources* 247 (2014): 703–711, https://doi.org/10.1016/j.jpowsour.2013.08.136.

10. A. Débart, L. Dupont, R. Patrice, and J. M. Tarascon, "Reactivity of Transition Metal (Co, Ni, Cu) Sulphides versus Lithium: The Intriguing Case of the Copper Sulphide," *Solid State Sciences* 8 (2006): 640–651.

11. J. Liu, Y. Wen, Y. Wang, P. A. van Aken, J. Maier, and Y. Yu, "Carbon-Encapsulated Pyrite as Stable and Earth-Abundant High Energy Cathode Material for Rechargeable Lithium Batteries," *Advanced Materials* 26 (2014): 6025–6030, https://doi.org/10.1002/adma.201401496.

12. G. A. Ferrero, G. Åvall, K. A. Mazzio, et al., "Co-Intercalation Batteries (CoIBs): Role of TiS_2 as Electrode for Storing Solvated Na Ions," *Advanced Energy Materials* 12 (2022): 2202377.

13. M. Pavan, K. Münch, S. L. Benz, et al., "Role and Evolution of FeS_2 Cathode Microstructure in Argyrodite-Based All-Solid-State Lithium–Sulfur Batteries," *Chemistry of Materials* 37 (2025): 3185–3196, https://doi.org/10.1021/acs.chemmater.4c03315.

14. J. Chen, T. Sun, J. Liu, et al., "Recent Advances on Transition Metal Sulfides for Key Components of Lithium–Sulfur Batteries," *Advanced Science* 12 (2025): 12191, https://doi.org/10.1002/advs.202512191.

15. F. Klein, B. Jache, A. Bhide, and P. Adelhelm, "Conversion Reactions for Sodium-Ion Batteries," *Physical Chemistry Chemical Physics* 15 (2013): 15876–15887, https://doi.org/10.1039/C3CP52125G.

16. M. S. Whittingham, "Ultimate Limits to Intercalation Reactions for Lithium Batteries," *Chemical Reviews* 114 (2014): 11414–11443, https://doi.org/10.1021/cr5003003.

17. G. Whang, L. Ketter, T. Zhao, E. Nazmutdinova, M. A. Kraft, and W. G. Zeier, "High Areal Capacity Cation and Anionic Redox Solid-State Batteries Enabled by Transition Metal Sulfide Conversion," *ACS Applied Materials & Interfaces* 16 (2024): 42189–42197, https://doi.org/10.1021/acsami.4c07252.

18. G. Whang and W. G. Zeier, "Transition Metal Sulfide Conversion: A Promising Approach to Solid-State Batteries," *ACS Energy Letters* 8 (2023): 5264–5274, https://doi.org/10.1021/acsenergylett.3c02246.

19. Z. Zhang, K. Dong, K. A. Mazzio, et al., "Phase Transformation and Microstructural Evolution of CuS Electrodes in Solid-State Batteries Probed by in Situ 3D X-Ray Tomography," *Advanced Energy Materials* 13 (2022): 2203143.

20. S. R. Hall and J. M. Stewart, "The Crystal Structure Refinement of Chalcopyrite, $CuFeS_2$," *Acta Crystallographica Section B Structural Crystallography and Crystal Chemistry* 29 (1973): 579–585, https://doi.org/10.1107/S0567740873002943.

21. A. L. Santhosha, N. Nazer, R. Koerver, et al., "Macroscopic Displacement Reaction of Copper Sulfide in Lithium Solid-State Batteries," *Advanced Energy Materials* 10 (2020): 2002394, https://doi.org/10.1002/aenm.202002394.

22. S. Senkale, S. Indris, M. Etter, and W. Bensch, "$CuFeS_2$ as a Very Stable High-Capacity Anode Material for Sodium-Ion Batteries: A Multimethod Approach for Elucidation of the Complex Reaction Mechanisms during Discharge and Charge Processes," *ACS Applied Materials & Interfaces* 13 (2021): 26034–26045, https://doi.org/10.1021/acsami.1c04946.

23. A. L. Santhosha, L. Medenbach, J. R. Buchheim, and P. Adelhelm, "The Indium–Lithium Electrode in Solid-State Lithium-Ion Batteries: Phase Formation, Redox Potentials, and Interface Stability," *Batteries & Supercaps* 2 (2019): 524–529, https://doi.org/10.1002/batt.201800149.

24. T. Shi, Q. Tu, Y. Tian, et al., "High Active Material Loading in all-Solid-State Battery Electrode via Particle Size Optimization," *Advanced Energy Materials* 10 (2019): 1902881.

25. G. Manthilake, J. Chantel, J. Monteux, et al., "Thermal Conductivity of FeS and Its Implications for Mercury's Long-Sustaining Magnetic Field," *Journal of Geophysical Research: Planets* 124 (2019): 2359–2368, https://doi.org/10.1029/2019JE005979.

26. H. Xie, X. Su, Y. Yan, et al., "Thermoelectric Performance of $CuFeS_{2+2x}$ Composites Prepared by Rapid Thermal Explosion," *NPG Asia Materials* 9 (2017): 390, https://doi.org/10.1038/am.2017.80.

27. A. Eakambaram, M. A. Saibalaji, and P. B. Sethupathi, "Role of Solid Lubricants/Sulfide Mix in Brake Performance for Automotive Applications—A Review," *Proceedings of the Institution of Mechanical Engineers, Part E: Journal of Process Mechanical Engineering* (2022): 09544089221110982, https://doi.org/10.1177/09544089221110982.

28. P. BalÁž, ed., *Process Metallurgy*, (Elsevier, 2000), 35.

29. M. G. Boebinger, D. Yeh, M. Xu, et al., "Avoiding Fracture in a Conversion Battery Material through Reaction with Larger Ions," *Joule* 2 (2018): 1783–1799, https://doi.org/10.1016/j.joule.2018.05.015.

30. Y. Wang, X. Li, Y. Zhang, X. He, and J. Zhao, "Ether Based Electrolyte Improves the Performance of $CuFeS_2$ Spike-Like Nanorods as a Novel Anode for Lithium Storage," *Electrochimica Acta* 158 (2015): 368–373, https://doi.org/10.1016/j.electacta.2015.01.141.

31. J. Zou, Z. Wu, R. Tang, Z. Ren, X. Niu, and L. Wang, "Copper Diffusion Related Phase Change and Voltage Decay in CuS Cathode," *Nano Research* 16 (2023): 8497–8503, https://doi.org/10.1007/s12274-023-5627-9.

32. J. Cabana, L. Monconduit, D. Larcher, and M. R. Palacin, "Beyond Intercalation-Based Li-Ion Batteries: The State of the Art and Challenges of Electrode Materials Reacting through Conversion Reactions," *Advanced Materials* 22 (2010): E170, https://doi.org/10.1002/adma.201000717.

33. J. Zou, J. Zhao, B. Wang, et al., "Unraveling the Reaction Mechanism of FeS_2 as a Li-Ion Battery Cathode," *ACS Applied Materials & Interfaces* 12 (2020): 44850–44857, https://doi.org/10.1021/acsami.0c14082.

34. H. Kim, H. N. Choi, J. Y. Hwang, C. S. Yoon, and Y. K. Sun, "Tailoring the Interface between Sulfur and Sulfide Solid Electrolyte for High-Areal-Capacity All-Solid-State Lithium–Sulfur Batteries," *ACS Energy Letters* 8 (2023): 3971–3979, https://doi.org/10.1021/acsenergylett.3c01473.

35. S. Conejeros, P. Alemany, M. Llunell, V. Sánchez, J. Llanos, and L. Padilla-Campos, "Structural Stability of Quaternary $ACuFeS_2$ (A = Li, K) Phases: A Computational Approach," *Inorganic Chemistry* 51 (2012): 362–369, https://doi.org/10.1021/ic201758j.

36. T. Bernges, L. Ketter, B. Helm, M. A. Kraft, K. A. See, and W. G. Zeier, "Transport Characterization of Solid-state Li_2FeS_2 Cathodes from a Porous Electrode Theory Perspective," *EES Batteries* 1 (2025): 172–184, https://doi.org/10.1039/D4EB00005F.

37. A. G. Hailemariam, Z. Syum, T. T. Mamo, et al., "Oxygen-Incorporated Lithium-Rich Iron Sulfide Cathodes for Li-Ion Batteries with Boosted Material Stability and Electrochemical Performance," *Chemistry of Materials* 36 (2024): 9370–9379, https://doi.org/10.1021/acs.chemmater.4c00508.

38. C. D. Wei, H. T. Xue, X. D. Zhao, and F. L. Tang, "Insights into the Electrochemical Properties of Li_2 FeS_2 after FeS_2 Discharging," *Physical Chemistry Chemical Physics* 25 (2023): 8515–8523, https://doi.org/10.1039/D2CP05930D.

Supporting Information

Additional supporting information can be found online in the Supporting Information section.

Supporting File: adfm76585-sup-0001-SuppMat.docx.